Chapter IV: Effect of size on cation distribution and magnetic transitions of $CoCr_2O_4$.

4.1. Introduction

The competition between structural and magnetic length-scales which gives rise to a range of new magnetic phenomena, are intensively studied by researchers when size of the particle is reduced to nanometer. The general question arises what happens to the bulk properties of a macroscopic body as one or more of its dimensions are reduced to atomic size. Chromites, having normal spinel structure, where Co^{2+} ions occupy A site and Cr^{3+} ions strongly prefer the B site, show very different magnetic transitions compared to ferrites. Cobalt chromite ($CoCr_2O_4$), exhibits a rich sequence of magnetic transitions such as paramagnetic to collinear ferrimagnetic ordering at Curie temperature, T_C (94K) and non-collinear spin-spiral ordering at T_S, 23K and finally to a lock-in transition, T_L, 15K. With decreasing temperature from 300K in chromites, the consequence of high crystal field stabilization energy of Cr^{3+} (2.02 eV) which leads to strong anti-ferromagnetic B-B interaction over A-B [Dwight et al. 1969]. As a result, the anti-ferromagnetic alignment between A and B sites is completely destroyed and system exhibits a screw ordering. This is otherwise named as ferrimagnetic spiral wherein the spins lie on the conical surfaces. Menuk *et al*. have shown in bulk sample that below T_C, magnetic ordering consists of a ferrimagnetic component and a spiral component through neutron diffraction and magnetic measurements [Menuk et al. (1964)]. The ferrimagnetic component exhibits long range order at all temperatures below T_C while the spiral component exhibits a short range order. The spiral component induces electric polarization and also a spontaneous magnetization for which it is said to be as multiferroic. Tomiyasu *et al*. revisited the spiral ordering by neutron scattering and

magnetic measurements in $CoCr_2O_4$ single crystals [Tomiyasu et al. (2004)]. They have shown a simultaneous formation of long range ferrimagnetic component and a short range spiral component as lowest temperature phase. It develops an incommensurate short range order below 50 K. Severance *et al.* have shown that with increase in temperature from 10 to 45K, intensity of the magnetic satellite peak decreases [Severance et al. (1993)]. At 50 K, the intensity of the diffused peak diminishes to the background level, indicating that short-range magnetic order is completely vanished.[8] Incommensurate to commensurate transition of the propagation vector is observed at spiral ordering temperature by Plumier *et al.* [Plumier et al. 1968]. Yamasaki *et al*. investigate that the compound undergoes a transition to a conical spin structure with an incommensurate propagation vector at T_S=26 K, and a lock-in transition at around 15 K [Yamasaki et al. (2006)]. Moreover, scarce reports on $CoCr_2O_4$ generates a lot of dispute on magnetic transitions i.e. whether short range or long range, spiral ordering is whether commensurate or incommensurate etc. The present study highlights the rich sequence of magnetic transitions in $CoCr_2O_4$ by reducing the size to 10 and 50 nm.

We have discussed the microstructure of 10 and 50 nm $CoCr_2O_4$ nanoparticles in section 4.2.1.Section 4.2.2 discusses the magnetic properties. The results are summarized in section 4.3.

4.2. Results

4.2.1. Structural and Microstructural analysis

4.2.1.1. X-ray Diffraction

Fig. 4.2.1 depicts the XRD pattern of $CoCr_2O_4$ calcined at 500^{o}C and 900^{o}C. The XRD patterns are fitted by standard fullprof profile fitting with Fd-3m space group (Rietveld method) using Fullprof program.

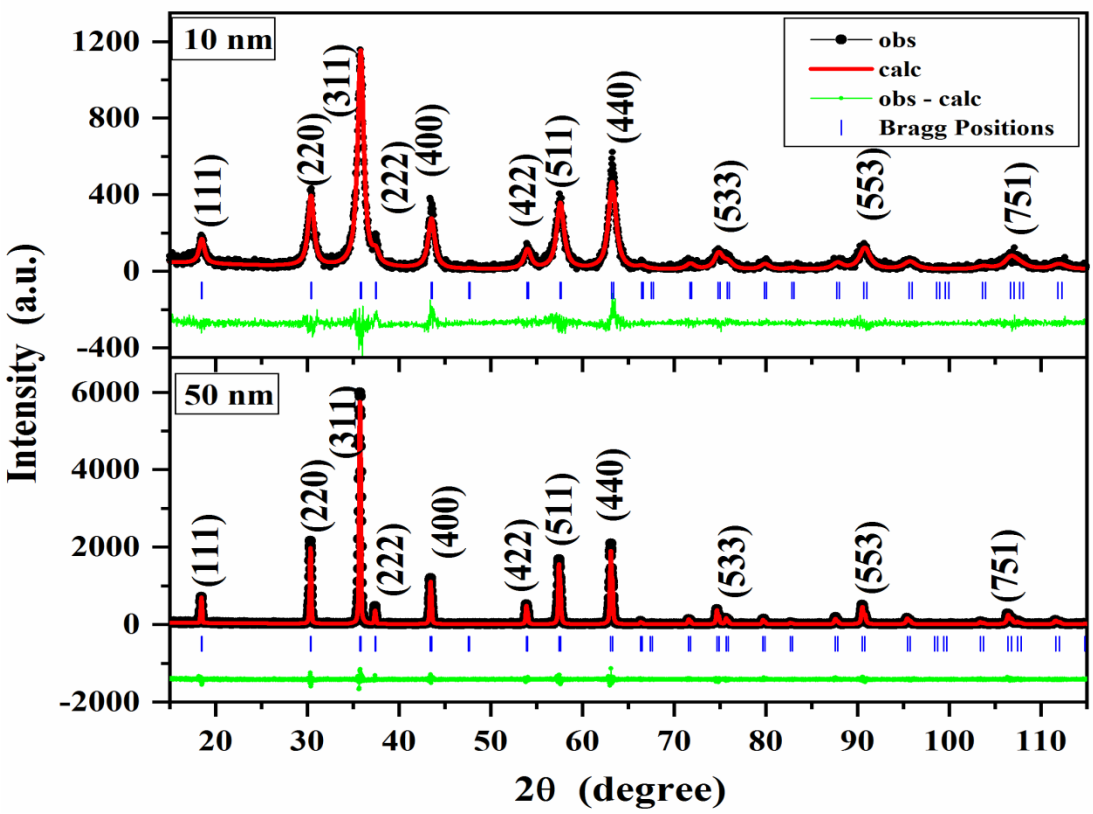

Fig. 4.2.1 X-ray diffraction (XRD) pattern of $CoCr_2O_4$ calcined at 500°C and 900°C fitted using Fullprof program.

The observed pattern, calculated data after fitting and the difference pattern between observed and calculated one are shown as dots, continuous line and as bottom line respectively. The tick marks above the difference plot show the positions of the Bragg peaks. The well defined peaks corresponding to Miller indices (111), (220), (311), (400), (422), (511) and (440) are ascribed to cubic phase of $CoCr_2O_4$ (JCPDS file no.:780711). No peaks other than $CoCr_2O_4$ corresponding to secondary phases have been observed in both samples. The lattice parameters of samples calcined at 500°C and 900°C are found to be 8.319±0.002 Å and 8.334±0.003 Å. The lattice parameter of later sample is in agreement with the bulk value [Lawes et al. (2006)]. The mean crystallite diameter estimated by using Scherrer formula after correcting the instrumental broadening are

along (311) are found to be ~ 10 and 50 nm for sample calcined at 500^{o}C and 900^{o}C respectively. The crystallite diameters are used as the nanoparticles average size in rest of the manuscript. The u parameter, a measure of oxygen position in fcc lattice, is obtained from Rietveld fitting found to decrease from 0.264 Å to 0.260 Å with increase in crystallite size and the later value is comparable to the ideal value of u (0.26Å) in polycrystalline bulk sample [Lawes et al. (2006)].This indicates that 50 nm particles evolves towards a more symmetric structure.

4.2.1.2 Scanning electron microscope

Field emission scanning electron micrographs of 10 nm and 50 nm samples are shown in Fig. 4.2.2 (a) and (b) respectively.

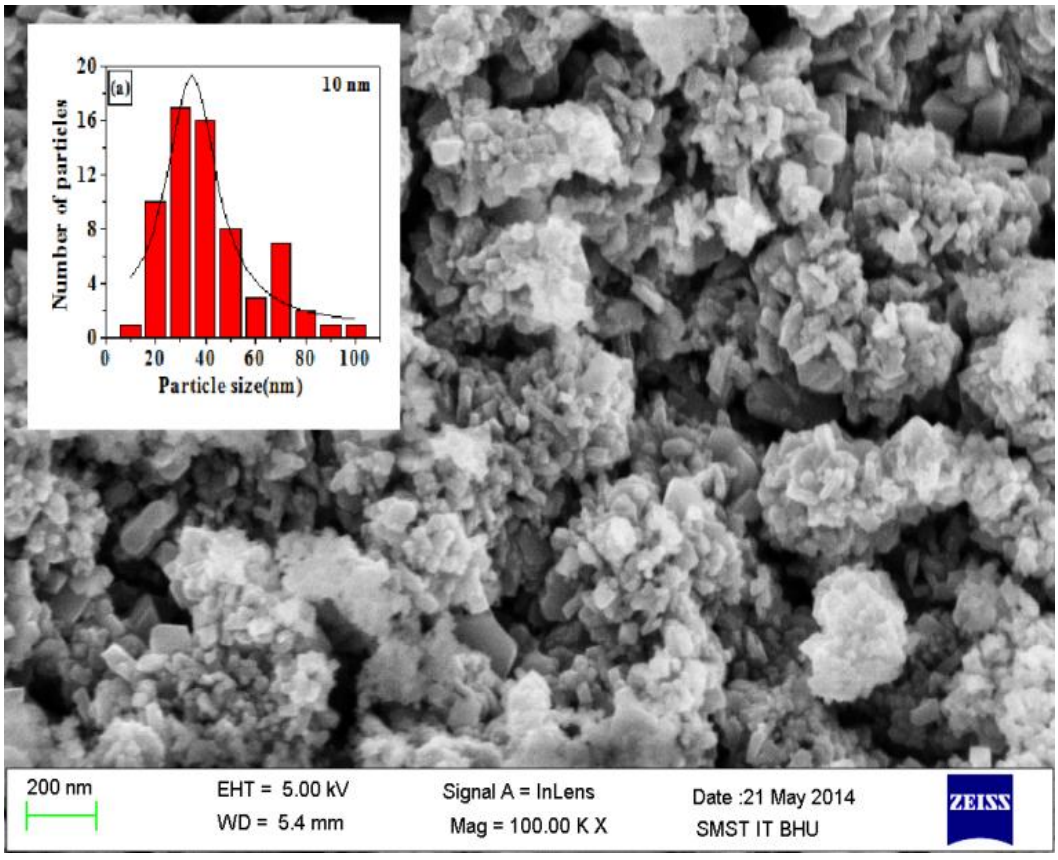

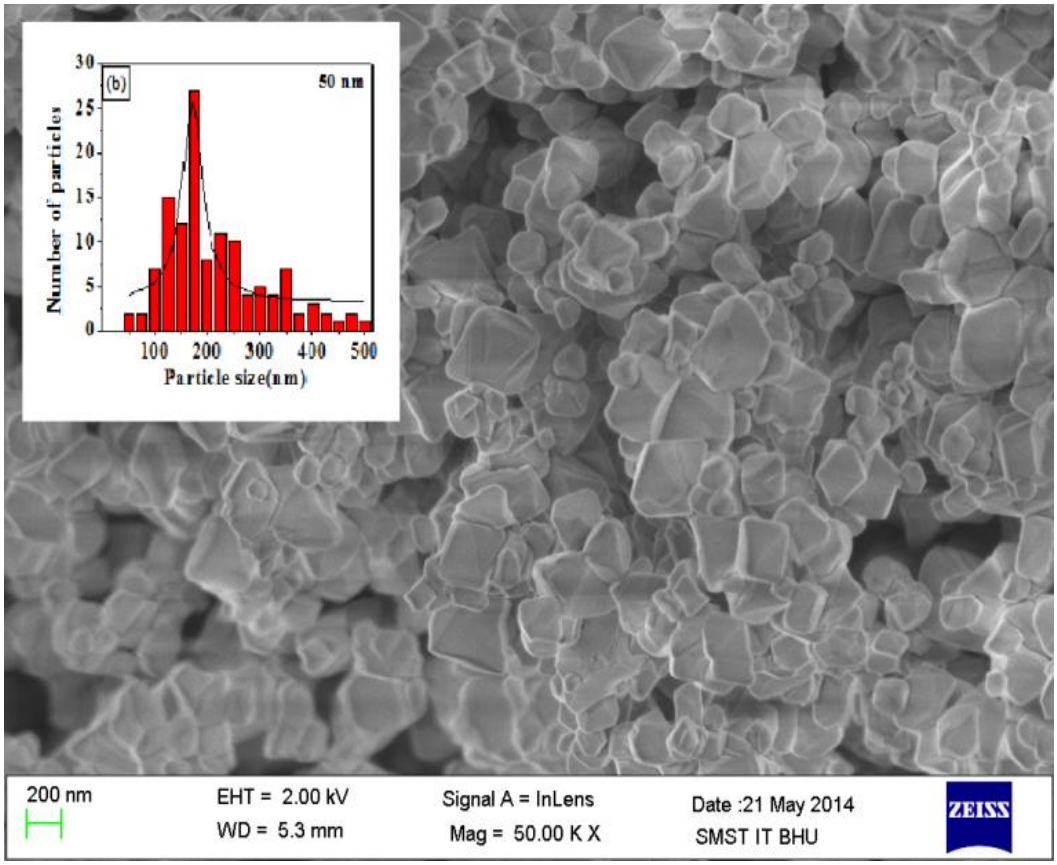

Fig. 4.2.2 High resolution Scanning Electron Micrograph of (a) 10 nm sample and (b) 50 nm sample of $CoCr_2O_4$. Insets show the corresponding particle size distribution histogram.

While the particles are of rectangular shape in 500^{o}C calcined sample, in 900^{o}C calcined sample the particles grow into trapezoidal shape. Both micrographs clearly indicate that the particles are agglomerated. Particle size distribution is calculated from SEM images using Image-J software and fitted with Lorentzian distribution function. The results are shown as inset of Fig. 4.2.2 (a) and (b). From figure, it is observed that majority of particles are found to be in 30-40 nm and 150-160 nm in 10 nm and 50 nm samples respectively. Comparing the average crystallite size obtained from Scherrer formula and particle size from SEM analysis, it is confirmed that the particles are polycrystalline in nature. In spinel ferrites, cations among A and B sites are redistributed irrespective of

their preferential site by reducing the size to nanometer range [Tang et al. (1991)]. In order to examine the distribution of Co and Cr among A and B sites, in cobalt chromite, we have undertaken x-ray absorption spectroscopy.

4.2.1.3 EXAFS Analysis

The data recorded at Co and Cr K edges are analyzed using Athena and Artemis programs coupled with FEFF 8.0 code for both samples. The data from 2 to 15.8 A^{-1} for both samples are weighted by k^3 uniformly after trying for k^2 and k^3 weighting schemes. It has been observed that the first coordination shell consisting of tetrahedrally or octahedrally coordinated oxygen atoms is best fitted when k^3 weighting scheme is used. Fig. 4.2.3 depicts the normalized absorbance vs. energy plots of Co & Cr K-edge in 10 nm and 50 nm samples.

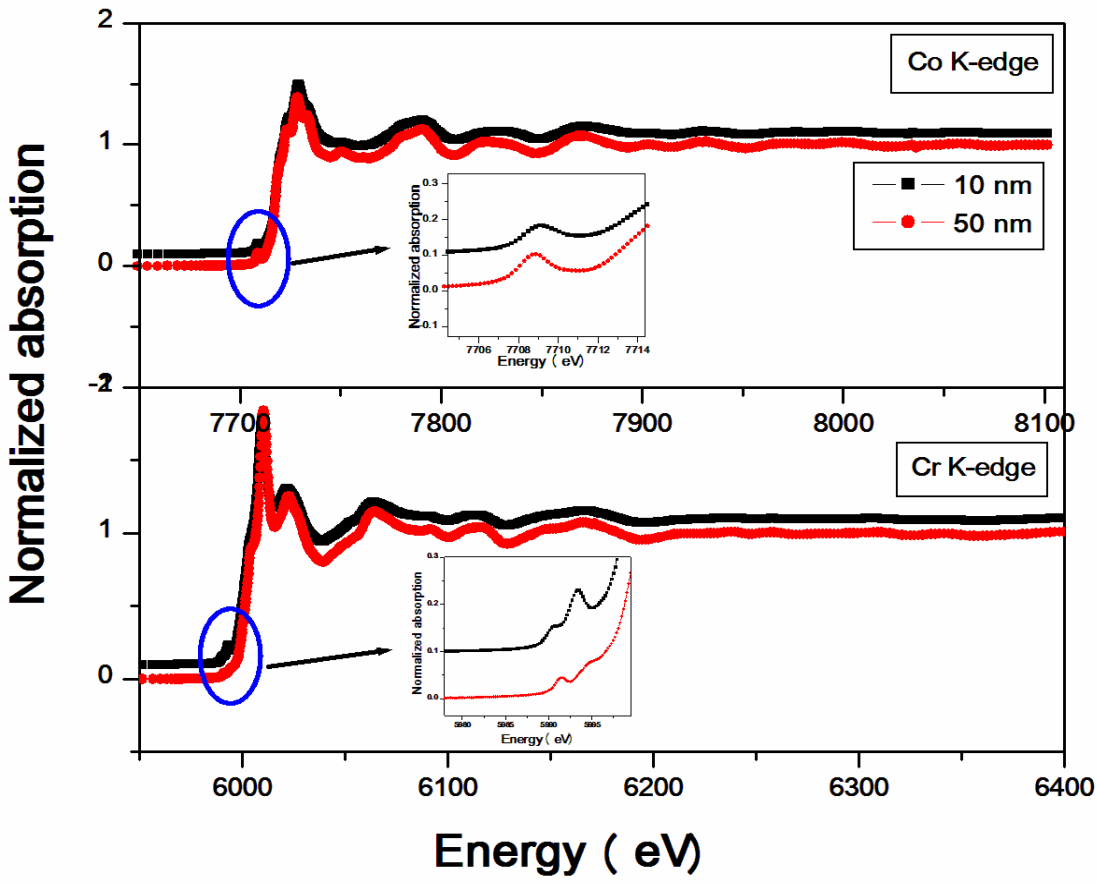

Fig. 4.2.3 Comparison of the EXAFS spectra of Co & Cr K-edge in 10 and 50 nm samples.

While the main peak is attributed to 1s to 4p transition, a small pre-edge peak observed in all spectra is due to 1s to 3d transition [Groot et al. (2001)].The inset of Fig. 4.2.3 shows the enlarged view of the pre-edge peak confirm the 1s to 3d quadruple transition. The pre edge peak intensity increases in tetrahedral symmetry due to local mixing of 4p and 3d orbital, which is found to be forbidden in octahedral symmetry due to inversion reported by Akthar *et al* [Akthar et al. (2009)]. The intensity of the pre-edge peak in the present case does not increase showing the evidence of absence of mixing of 4p and 3d orbital. Results show that the near edge structure is identical for both the samples. Fig. 4.2.4

shows the comparison of the Fourier transform in r space showing radial distribution of atoms around Co and Cr respectively.

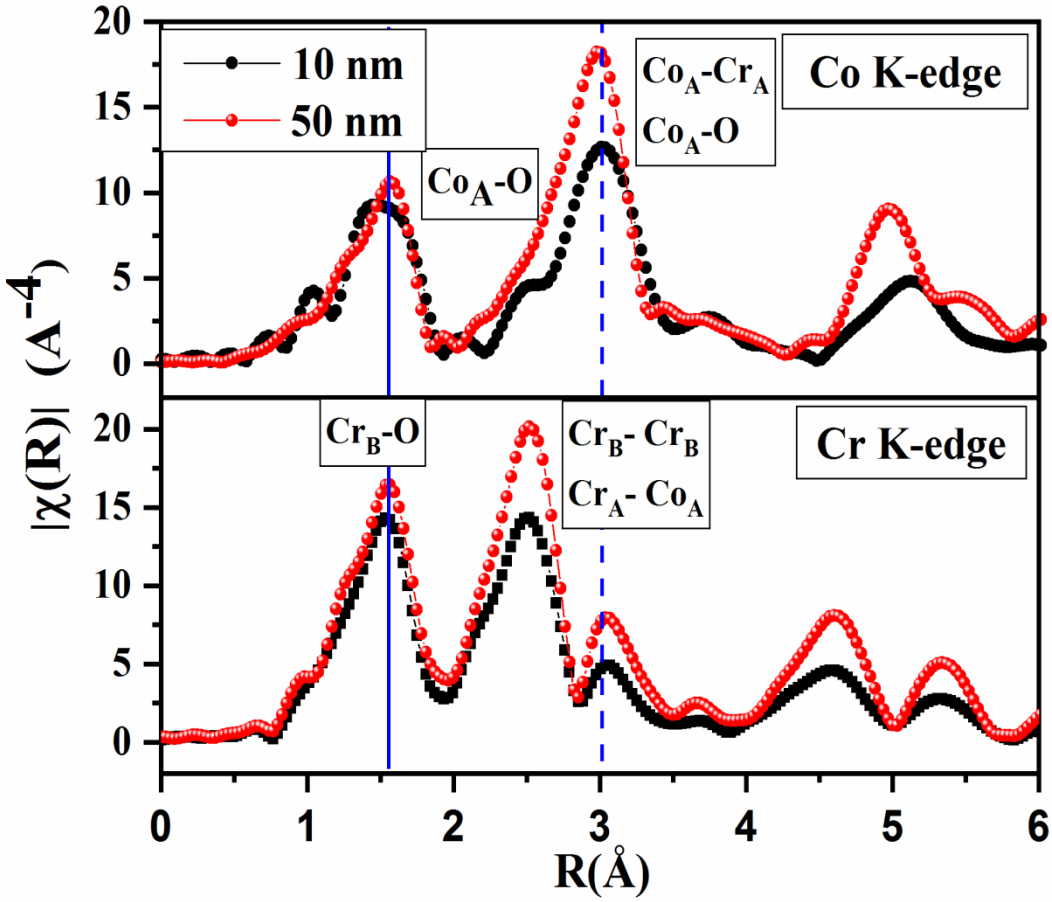

Fig. 4.2.4 Fourier transformed Co & Cr K-edge of the 10 and 50 nm samples of the EXAFS for illustrating pair correlations.

As $CoCr_2O_4$ crystallizes in normal spinel structure with Co preferring tetrahedral site (A-site) and Cr occupying octahedral site (B-site), we have calculated the partial radial distribution function using FEFF code resulting into single scattering paths tabulated in Table 4.1.

Table 4.1: Bond length (r), disorder factor (σ^2) obtained by EXAFS fitting for 10 nm and 50 nm samples at Co K edge and Cr K edge.

10 nm sample					
Co K-edge	r (Å)	σ^2	Cr K-edge	r (Å)	σ^2
Co-O	1.960(17)	0.007(1)	Cr-O	1.982(4)	.0065(6)
Co-Cr	3.454(18)	0.009(2)	Cr-Cr	2.960(7)	0.008(1)
Co-O	3.43(9)	0.047(23)	Cr-Co	3.480(27)	0.013(2)
Co-Co	3.569(40)	0.009(6)	Cr-O	3.705(57)	0.011(10)
E_f=1.16 eV R=0.0007 N=0.89			E_f=-7.4 eV R=0.0001 N=0.98		
50 nm sample					
Co K-edge			Cr K-edge		
Co-O	1.972(2)	0.006(6)	Cr-O	1.986(6)	0.0063(6)
Co-Cr	3.48(2)	0.008(1)	Cr-Cr	2.959(7)	0.0067(7)
Co-O	3.418(6)	0.010(6)	Cr-Co	3.468(9)	0.010(1)
Co-Co	3.631(6)	0.007(1)	Cr-O	3.72(9)	0.02(2)
E_f=1.14 eV R=0.0002 N=0.96			E_f=-7.8 eV R=0.0002 N=1.12(9)		

Where, E_f is the energy shift parameter.

Although, the distribution of cations at two sites can be differentiated by the radial distance of the first coordination shell in most of the ferrites, in $CoCr_2O_4$, the radial distribution of first coordination shell in the two environments is nearly same. Hence, it could not be used in this particular case as a finger print of tetrahedral or octahedral coordination (see Table 4.1). However, the position of second peak in the fourier transform i.e. the cation-cation distance in second coordination shell is remarkably different, is therefore a good signature for determining the distribution of cations in two different environments. For better comparison, the Fourier transformed Co and Cr EXAFS for 10 and 50 nm samples are plotted in Fig. 4.2.4. For Co k-edge and Cr k-edge, we note that there is one peak at ~1.6Å which is due to the first shell of oxygen atoms. The second peak at ~3 Å is due to the second coordination shell. Similarly for Cr, the first peak is at 1.55 Å is due to the first shell of oxygen atoms and the second peak at 2.5

Å is due to second coordination shell. The dashed line is used to mark the difference between 2nd coordination shell of Co and Cr-edge. It clearly gives an indication that the two cations occupy different environment and if any mix site occupancy is present, it is outside the detection limit of this technique. From Fig. 4.2.4, it is clearly seen that when the particle size is reduced, it is not affecting the first coordination shell. However, reduction in the intensity of the second shell is due to surface effects [Camilla et al. (2008)]. It is important to note that visually there is no signature of changes found in site distribution of the two cations when the particle size is reduced. After getting the qualitative idea for the local structure around Co and Cr, we fit the reduced EXAFS data in r space. It is well known that σ^2, the amplitude function which is the mean-square displacement of the path length due to the thermal or static disorder is strongly correlated with the number of nearest neighbours. It is essential to find out the coordination number. In order to deduce the amplitude function for first coordination shell of Co and Cr edges, as per theoretical calculation, the intensity of the first coordination shell in Cr atom is taken roughly 1.5 times as compared to Co atom. Because, Cr is octahedrally coordinated and Co is tetrahedrally coordinated, the first coordination shell is thus fitted with fixed coordination number and floating amplitude function for the two edges simultaneously that resulted into σ^2 of 1.39. This value is then fixed for fitting all data sets. EXAFS spectra and Fourier transforms (both experimental and fitted models) of Co & Cr edge in r and k space are shown in Fig. 4.2.5 (a, b) and 4(c, d) respectively.

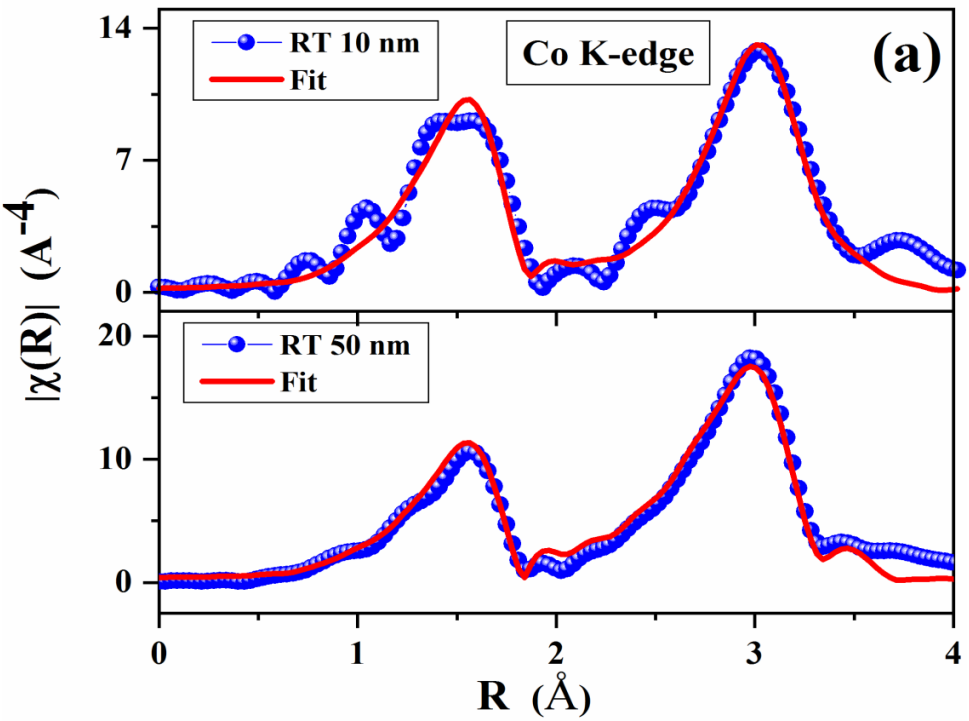
RT 10 nm
Fit
Co K-edge
(a)
RT 50 nm
Fit
|χ(R)| (A-4)
R (Å)

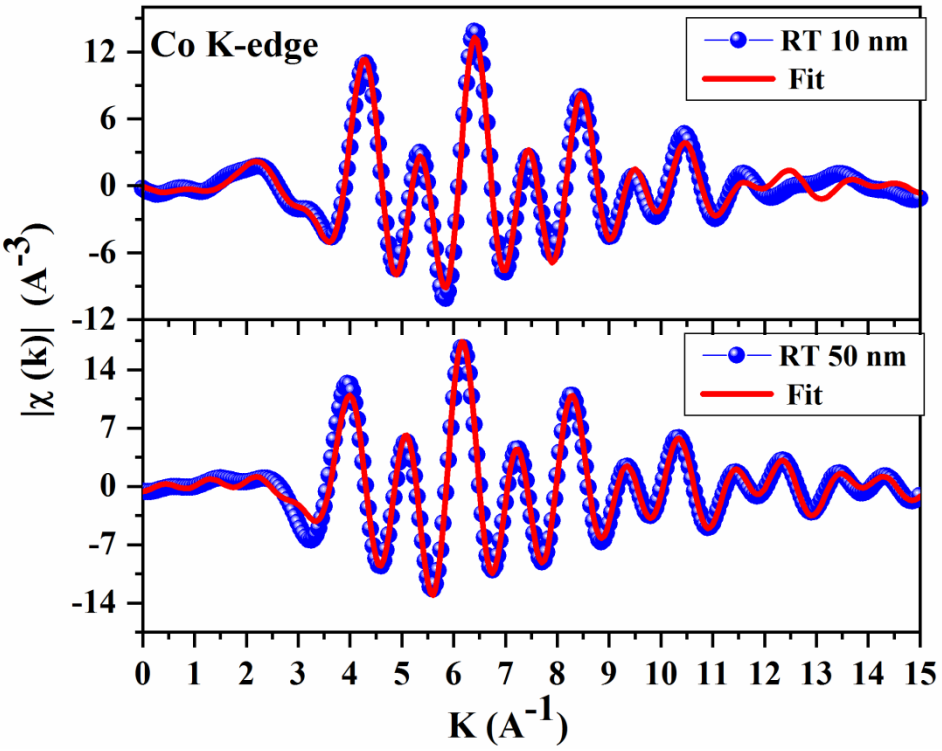
Co K-edge
RT 10 nm
Fit
RT 50 nm
Fit
|χ (k)| (A-3)
K (A-1)

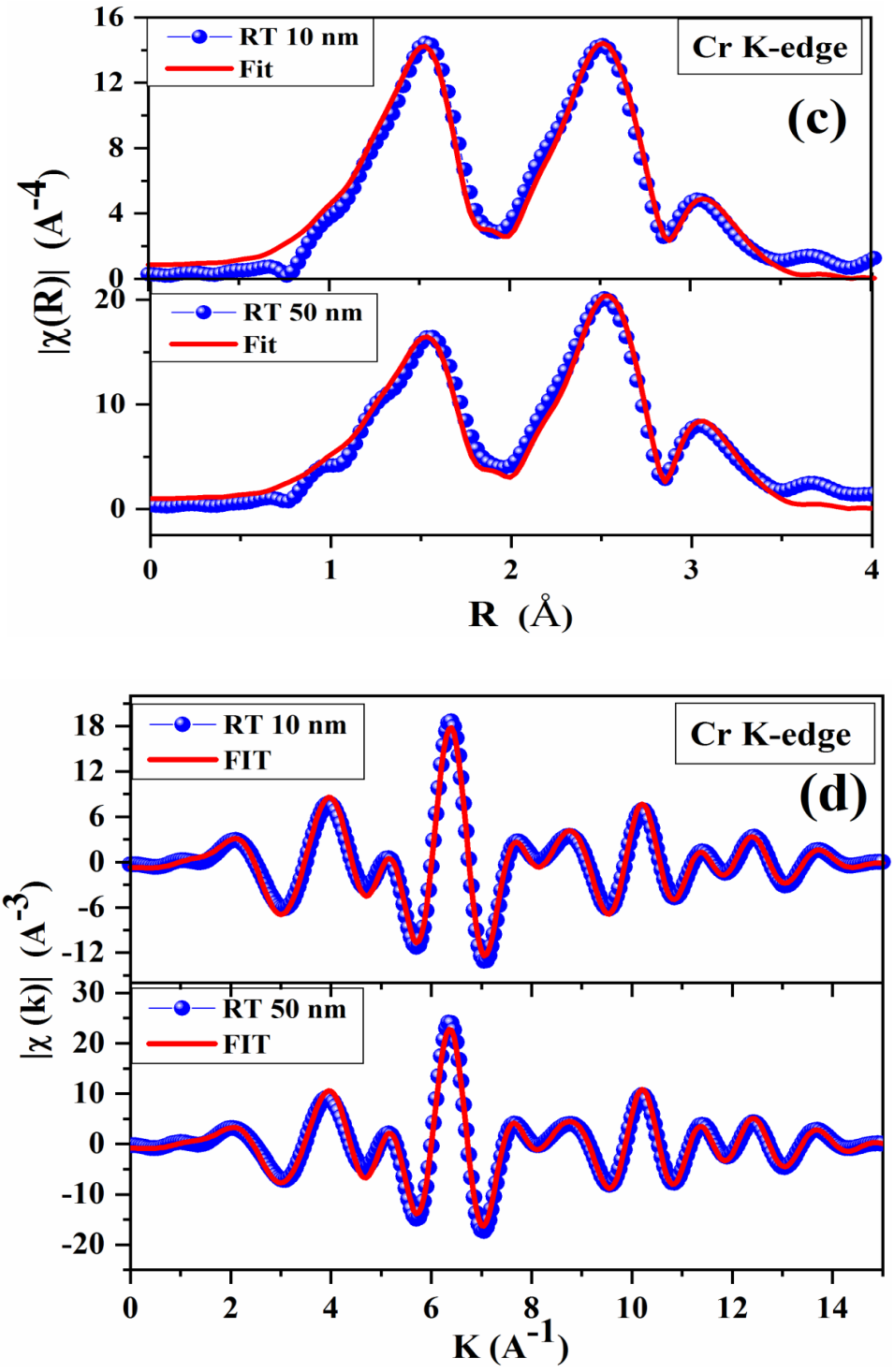

Fig. 4.2.5 (a) & (b) Co K-edge and **(c) & (d)** Cr K-edge Fourier transformed EXAFS data with magnitude, real and imaginary parts of the phase plotted with fitted curve for 10 nm and 50 nm samples.

Following standard fitting procedure, paths with relative amplitude of 10% or higher is considered which eliminates multiple scattering paths leaving only single scattering path.

Table 4.2: Correlation, Coordination number (CN), Bond length (r) and relative amplitude for tetrahedral and octahedral environment.

Correlation		**CN**	**r(Å)**	**Relative amplitude**
Tetrahedral Environment: central atom at A-site				
A1	Co-O	4	1.977	100
A2	Co-Cr	12	3.453	95
A3	Co-O	12	3.488	76
A4	Co-Co	4	3.607	24
Octahedral environment: Central atom at B-site				
B1	Cr-O	6	1.988	100
B2	Cr-Cr	6	2.945	27
B3	Cr-Co	6	3.453	27
B4	Cr-O	2	3.434	9
B5	Cr-O	6	3.668	23

The paths used in fitting with weightage of amplitude are given in Table 4.2. Fitting the data taking the calculated parameters, it is confirmed that like in bulk material, due to strong preferential occupancy of Cr^{3+} in B site, even after reducing the size to 10 and 50 nm, cation distribution does not change. Now, we proceed to examine magnetic properties by analyzing the field and temperature dependent magnetization in 10 and 50 nm samples.

4.2.2. Magnetic Properties

4.2.2.1. Temperature dependent magnetization

Temperature dependence of zero-field-cooled (ZFC) and field-cooled (FC) magnetization with applied field of 0.05, 0.5, 10, 50 kOe for 10 and 50 nm samples are depicted in Fig. 4.2.6 (a) and (b) respectively.

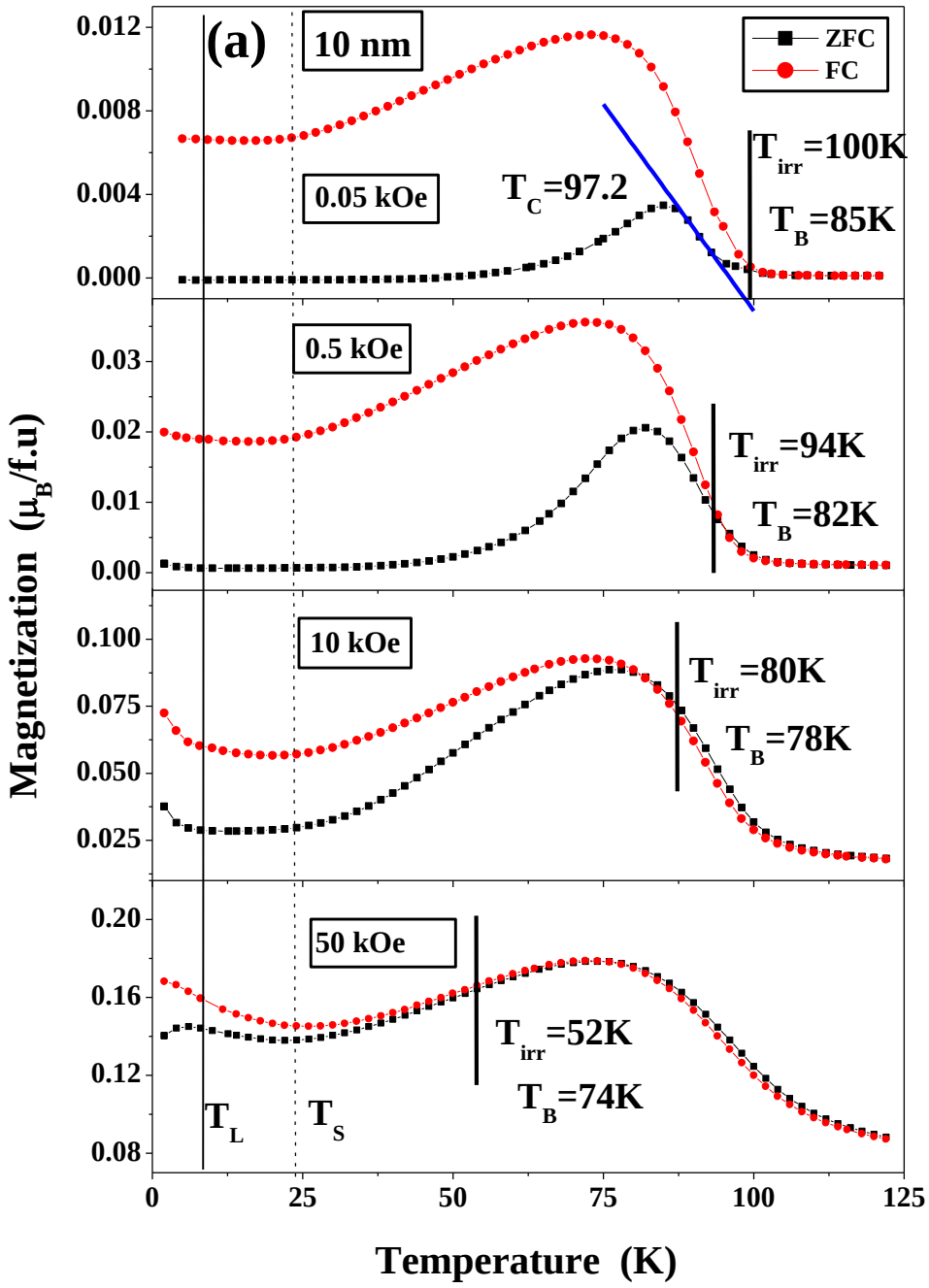
(a)
10 nm
ZFC
FC
0.05 kOe
T_C=97.2
T_{irr}=100K
T_B=85K
0.5 kOe
T_{irr}=94K
T_B=82K
10 kOe
T_{irr}=80K
T_B=78K
50 kOe
T_{irr}=52K
T_B=74K
T_L
T_S
Magnetization (μ_B/f.u)
Temperature (K)

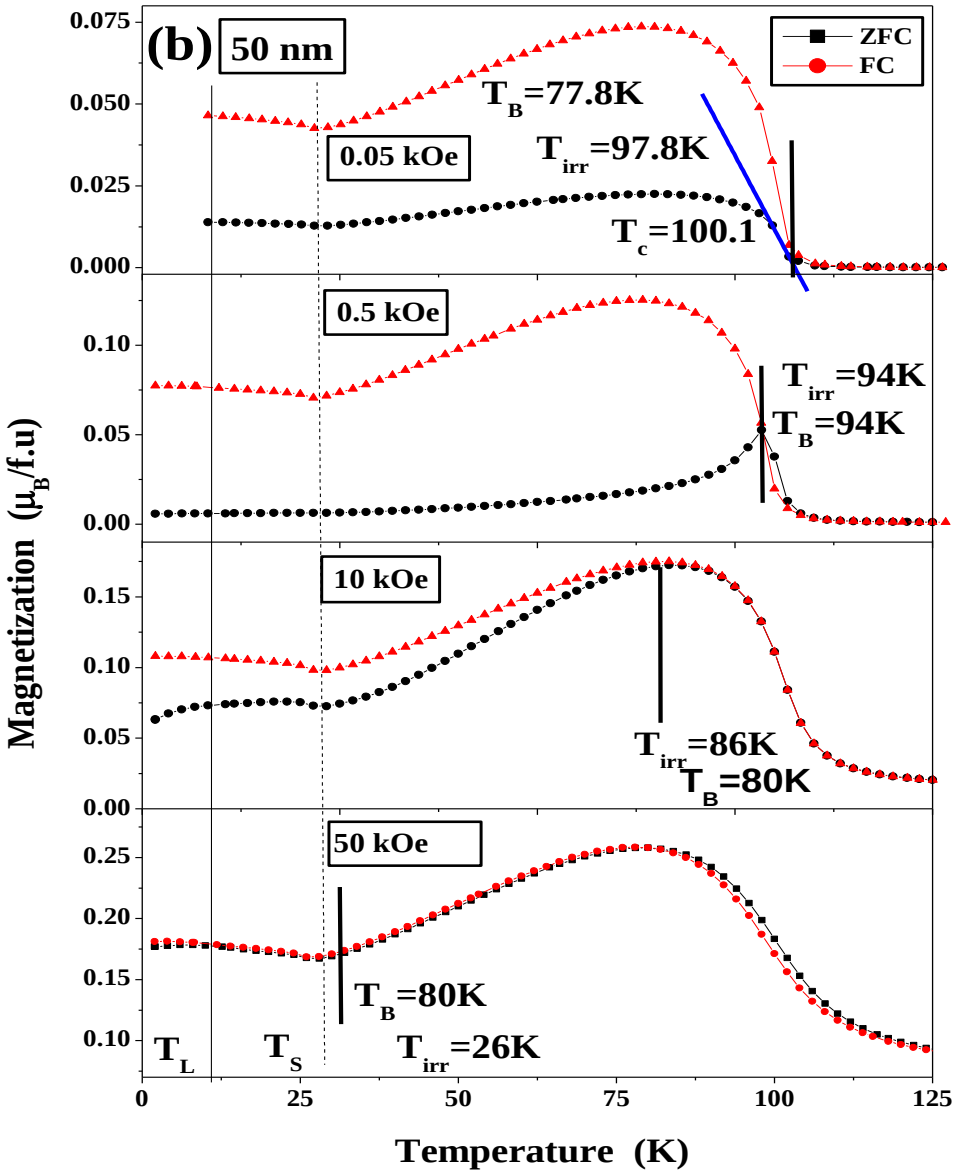

Fig. 4.2.6 Temperature dependent magnetization under zero field cooling (ZFC) and field cooling (FC) measured at different magnetic fields such as 0.05 kOe, 0.5 kOe, 10 kOe and 50 kOe for **(a)** 10 nm sample **(b)** 50 nm sample respectively. Solid line represents T_L and dashed line represents T_S.

With decreasing temperature, both M_{ZFC} and M_{FC} increase dramatically and show a maximum at specific critical temperature which is either blocking temperature T_b or spin freezing temperature, T_f. M_{ZFC} and M_{FC} curves split at a temperature named as irreversible temperature, T_{irr} which is either below or above T_b/T_f. T_b/T_f and T_{irr} shifts to lower temperature with increase in applied field in both samples upto 10 kOe. At 50 kOe field, while the bifurcation in M_{ZFC} and M_{FC} persists in 10 nm sample, in 50 nm, it is merged completely. The magnetization difference between M_{FC} and M_{ZFC} is found to be higher in 10 nm sample than in bulk cobalt chromite [Lawes et al. (2006)]. Above T_b, M_{ZFC} and M_{FC} drop sharply indicating long range ferrimagnetic to paramagnetic transition i.e. Curie temperature, T_C. T_C's are confirmed from first point of inflection in the first derivative of the magnetization (Fig. not shown here). The extrapolation of the linear part of M_{ZFC} intersects the temperature axis at 97.2, 99.4, 108.1 and 137.4 K; and at 100.1, 100.2, 105 and 125 K after applying field 0.05, 0.5, 10, 50 kOe respectively in 10 and 50 nm samples respectively (Fig. 4.2.6). In both 10 and 50 nm samples, T_C is found to be higher than that of bulk sample [Lawes et al. (2006)]. However, increase in T_C with size of the nanocrystalline particles follows the standard theory of finite system. With increase in applied field, T_C's are found to be increased in both cases as expected. However, one may note that significant difference in T_C is observed in both samples at 50 kOe which support the existence of bifurcation between M_{FC}& M_{ZFC} even at 2K. T_C is found to be higher than that of the T_C of single crystal (93 K) and polycrystalline sample (94 K) [Lawes et al (2006); Tomiyasu et al. (2004)]. A large increase in T_C has been reported by reducing the size to nanoscale range in similar spinel ferrites [Tang et al. (1991); Rath et al. (1999)]. Below T_C, M_{ZFC} and M_{FC} bifurcates followed by a large

increase in both ZFC and FC curves in both samples and then decreases further with decrease in temperature. An anomaly around a temperature ~25 ±1K, known as spiral ordering temperature (T_S) is observed irrespective of measurement field in 10 and 50 nm samples. T_S is shown as dashed line in Fig. 4.2.6 (a) and (b). Similar to our result, in single crystal Tomiyasu et al., and in bulk G. Lawes et al., have showed T_S from M vs. T measurement. Bhowmik *et al.* have shown suppression of T_S at high magnetic field (50 kOe) in nanoparticles of $MnCr_2O_4$ [Bhowmik et al. (2006)]. In bulk and single crystals of $CoCr_2O_4$, T_S is observed at 27 K and 25 K respectively which matches well with the T_S observed by us [Lawes et al. (2006); Yamasaki et al. (2006)]. Further decreasing the temperature, although magnetization saturates at lowest measurement temperature in 50 nm sample, increasing trend in magnetization is observed in 10 nm sample. We do not observe negative magnetization in M_{ZFC} as is found in bulk samples rather we observe an order of magnitude higher M_{FC} than in bulk [Lawes et al. (2006)]. Below T_S, another magnetic anomaly at 5 K and 8.5 K known as lock-in-transition is observed in 10 and 50 nm samples respectively. To the best of our knowledge, T_L has neither been observed in polycrystalline nor in nanoparticles except in single crystals [Lawes et al. (2006); Yamasaki et al. (2006); Kitani et al. (2013)]. As spiral ordering temperature is an indication of dominant $J_{B\text{-}B}$ interaction over $J_{A\text{-}B}$, it is confirmed that with reducing size, cation distribution is not affected corroborated with EXAFS results. Though M_{ZFC} shows a maximum for both superparamagnets and spin glasses, the temperature dependence of FC susceptibility becomes saturated below the maximum temperature for spin glasses and continues to increase below that temperature for superparamagnets [Bitoh et al.

(1995); Bedanta et al. (2009)]. The spin glass or superparamagnetic behavior of these nanocrystalline particles is further probed by ac susceptibility measurement.

4.2.2.2 Temperature dependent ac susceptibility

Temperature dependent ac susceptibility measured at several frequencies ranging from 3 to 1000 Hz probes further the spin glass (SG) and SPM behaviour. The sample is first cooled from room temperature down to 5 K in a zero magnetic field. Then a probing ac magnetic field of 3.0 Oe is applied to measure the susceptibility as the temperature is slowly raised. Fig. 4.2.7 (a) and (b) show the real and imaginary part of ac susceptibility for 10 nm and 50 nm samples respectively.

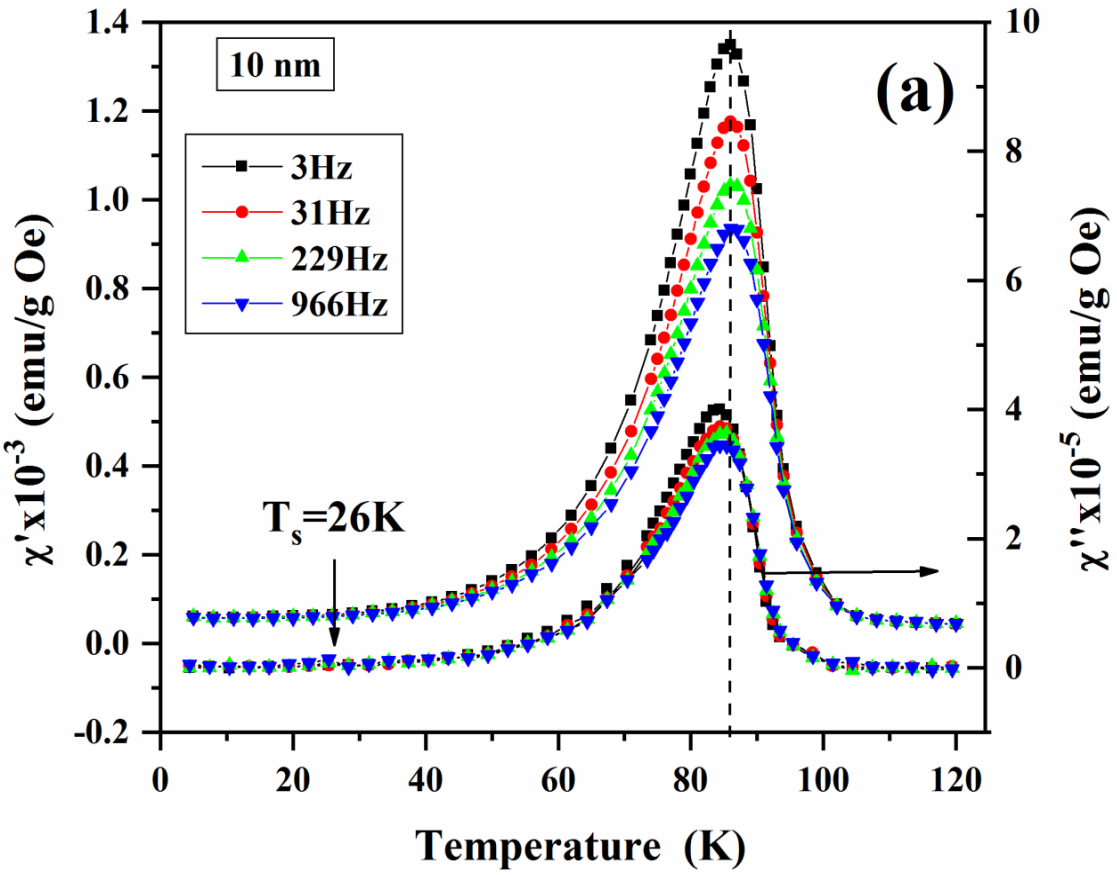

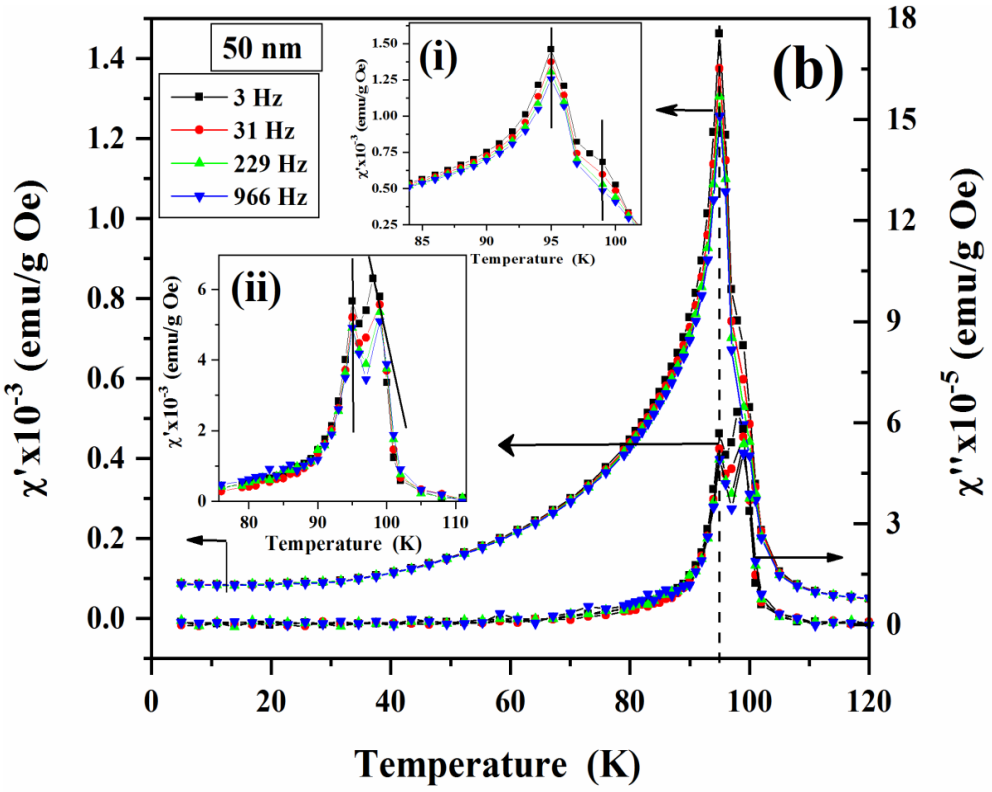

Fig. 4.2.7 (a) & (b) Real and imaginary parts of ac susceptibility versus temperature measured at 3 Oe field and at different frequencies such as 3, 31, 229 and 966 Hz for 10 nm and 50 nm samples respectively. Inset of Fig. 4.2.7 (a) show $\frac{d\chi''}{dT}$ vs. T for 966 Hz frequency. Insets (i & ii) of Fig. 4.2.7 (b) show the expanded view of the peak shift of real and imaginary part of ac susceptibility with increasing frequency.

Real part (χ') exhibits a broad peak similar to that of ZFC magnetization and peak position does not change with frequency in 10 nm sample except a decrease in χ'_{max}. In addition to shifting in χ'' with frequency, we also see an anomaly at ~ 26 K. Inset of Fig. 4.2.7 (a) shows $\frac{d\chi''}{dT}$ vs. T , where T_S is clearly shown. One may notice that, in 50 nm sample, though χ' does not show prominent splitting of the peak, χ'' splits into two

prominent peaks and the later peak position shifts towards higher temperature with increasing frequency (shown as inset of Fig. 4.2.7(b)). To identify the dynamic behaviour of the blocking/freezing process, the frequency dependent T_B fitted with an empirical relation [$\Phi=\frac{\Delta T_B}{T_B \Delta \log_{10} \omega}$] where Δ is the difference in related parameters. Φ value is found to be 0.004 which mostly matches with the typical value of spin glass [Mydosh et al. (1993)]. In addition to spin glass, the two peak behaviour is attributed to core-shell structure. Similar splitting of a.cχ'' into two sharp peaks observed in NiO surrounded by $Ni(OH)_2$ is ascribed to core shell structure [Godsell et al. (2011)]. While the former peak in the above is independent of frequency, the later one shifts with frequency as observed in the present case.

4.2.2.3 Memory effect

The evidence of spin-glass behaviour is further demonstrated by memory experiment. To perform memory effect in ZFC protocol, we have measured the ZFC magnetization in a standard way and is said to be as reference data. Then the sample is cooled down to 2 K in zero magnetic field with a stop of 10,000s (2.8 h) at 75 K. During subsequent heating the magnetization is measured up to 300 K by applying field of 50 Oe. Fig.4.2.8 (a) and (b) show the ZFC reference curve and ZFC memory curve for 10 nm and 50 nm samples respectively.

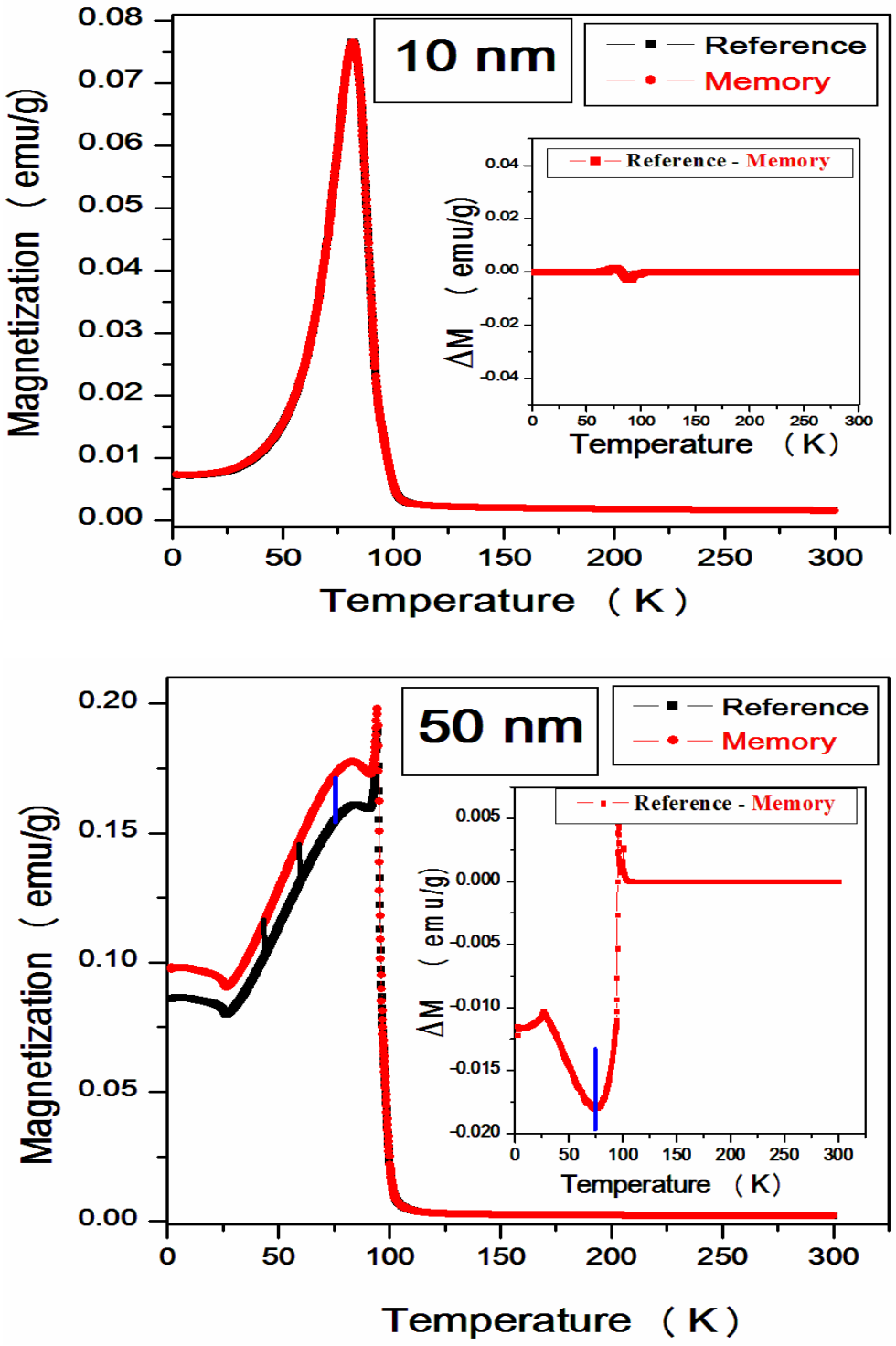

Fig. 4.2.8 (a) and (b) Experimental results of ZFC reference curve and ZFC memory curve for 10 nm and 50 nm samples respectively. Inset show the difference in magnetization of reference and memory data plotted as a function of temperature for corresponding samples.

Inset of corresponding figure show the difference between ZFC memory and reference data as a function of temperature. The dip observed at 75 K is resultant of memory effect i.e. the system remembers its thermal history when the temperature is returned to 75 K during heating. The memory effect found in ZFC of interacting magnetic nanoparticle system is an unequivocal signature of spin glass behavior which is observed in 50 nm sample. The core-shell structure is further examined by measuring magnetic field dependent magnetization.

4.2.2.4 Field dependent magnetization

Fig.4.2.9 (a) and (b) depict the magnetization (M) versus external magnetic field (H) for 10 nm and 50 nm samples which show non-saturation of magnetization upto 70 kOe irrespective of measurement temperature. At 95 K, magnetization readily increases at low field and then linearly increases up to 70 kOe showing small coercivity and remanence. The non-saturation of magnetization results from the large contribution of disordered spins at the surface, which always constitutes a good fraction in nanoparticles.

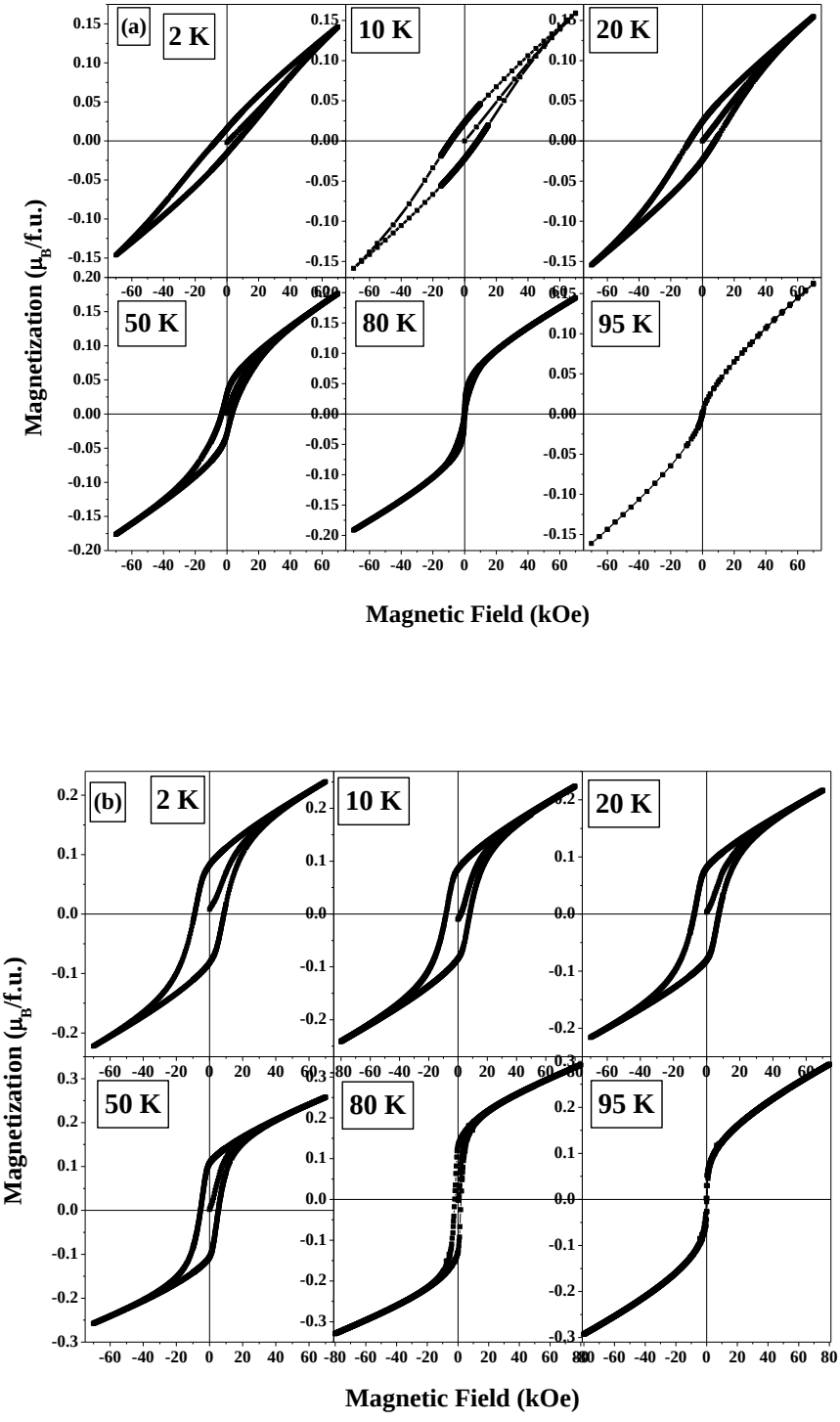

Fig. 4.2.9 Magnetic field (H) dependent Magnetization at 2 K, 10 K, 20 K, 50 K, 80 K, 95 K for **(a)** 10 nm sample and **(b)** 50 nm sample.

From Fig 4.2.9 (a) and (b), it is clearly shown that near T_C, the loop is s-shape, where H_c and M_r are minimum and changes to typical hysteresis with decreasing temperature down to 2 K**.** This also points toward a core shell structure where core spins showing a long range ferrimagnetic order and saturate at low field; disorder spins at the surface show a linear increase in magnetization upto higher field. Similar behaviour has been reported by Kodama *et al.* in $NiFe_2O_4$ nanoparticles where core spins are aligned ferrimagnetically and surface spins contribute to the spin glass below 50 K [Kodama et al. (1996)]. Yi *et al*. show through computational and experimental studies that nanoparticles of NiO exhibits uncompensated surface magnetization and shifted hysteresis loop due to core-shell structure [Yi et al. (2007)]. Nagornyi *et al.* experimentally estimated the shell thickness of spherical magnetic particles dispersed in liquid [Nagornyi et al. (2010)]. Verde *et al.* calculated the same in different ferrite nanoparticles [Verde et al. (2012)].The competition between core and surface spin alignment leads to change in the loop area which varies with size. M_s is found to be an order of magnitude less than that of theoretical magnetic moment of cobalt chromite ($3\mu_B$). The decrease in saturation magnetization with particle size is attributed to an increase in the proportion of non-collinear magnetic structure, in which the magnetic moments in the shell are not aligned with the direction of external magnetic field. It has also been reported by Coey *et al.* that reduced saturation magnetization could be due to disordered cation distribution among A and B sites which is discarded in our case [Coey et al. (1971)]. Because, we have not observed any change in cation distribution in nanocrystalline particles confirmed from EXAFS and unchanged T_S value. However, ferrites having similar spinel structure experiences redistribution of cations among A and B sites after reducing the size to

nanometer range [Rath et al. (2002)]. From Fig.4.2.9, one may notice that below 95 K, coercivity dramatically increases by an order of one or two compared to bulk H_c with decrease in temperature. Though above T_S, the initial magnetization responds readily and shows coercivity (H_c) of ~0.05 kOe in single crystals, we observe very high coercivity (~3-5 kOe) at 50 K in both samples. Below T_S, H_c increases by almost two fold (~7-9 kOe) which is an order of magnitude higher than in single crystal (750 Oe at 10 K) [Tomiyasu et al. (2004)]. Below T_S, the combination of spiral and ferrimagnetic ordering requires a larger field for the magnetic response of these nanocrystalline particles i.e. higher H_c. However, such high H_c is not only due to the above facts but also due to the strong disordered spins at the surface which is clearly evidenced from the non saturation of magnetization.

4.2.2.5 Diffused Neutron Scattering using polarized neutrons

The origin of rich sequence of magnetic ordering observed in nanocrystalline particles of $CoCr_2O_4$ is further probed by neutron scattering using polarized neutron beam. We have performed experiments with polarization analysis along three orthogonal directions in order to separate the magnetic, nuclear scattering component and also the spin-incoherent scattering background. The separate magnetic neutron scattering clearly displays the satellite magnetic Bragg peak at low temperature and further reveals that a part of the atoms in the samples remains disorder even at very low temperature resulting in a relatively flat diffuse background. Such diffuse background due to magnetic disorder has been proposed earlier by Golosovsky et al. [Golosovsky et al. (2001)]. They have reported that the finite-size effect in MnO nanoparticles shows a collective spin freezing at the surface due to the competition between exchange and anisotropy energies. But this

finite size effect could also play a significant role in cobalt chromite nanoparticles, since the super exchange magnetic bonds are very sensitive to any non-stoichiometry. The broken bond and the reduced oxygen coordination at the surface result into strong surface disorder. Temperature dependent magnetic Bragg peaks in the range of 3 K to 110 K are depicted in Fig.4.2.10. In both samples, the fundamental reflections are coherent Bragg reflections up to 90K, and at 110 K, intensity of (111) reflection diminishes to the background level. This indicates that the ferrimagnetic component exhibits long-range order below 110 K. With decreasing temperature from 110 K, (111) reflection in 10 nm sample is found to be very broad and asymmetric, whereas, in 50 nm sample, we have observed (111) and an additional satellite peak below 50 K. The diffused peak intensity in 10 nm sample increases as the temperature decreases and as a consequence, decreasing temperature reflects the growth of the polar clusters [La-Orauttapong et al. (2001)].

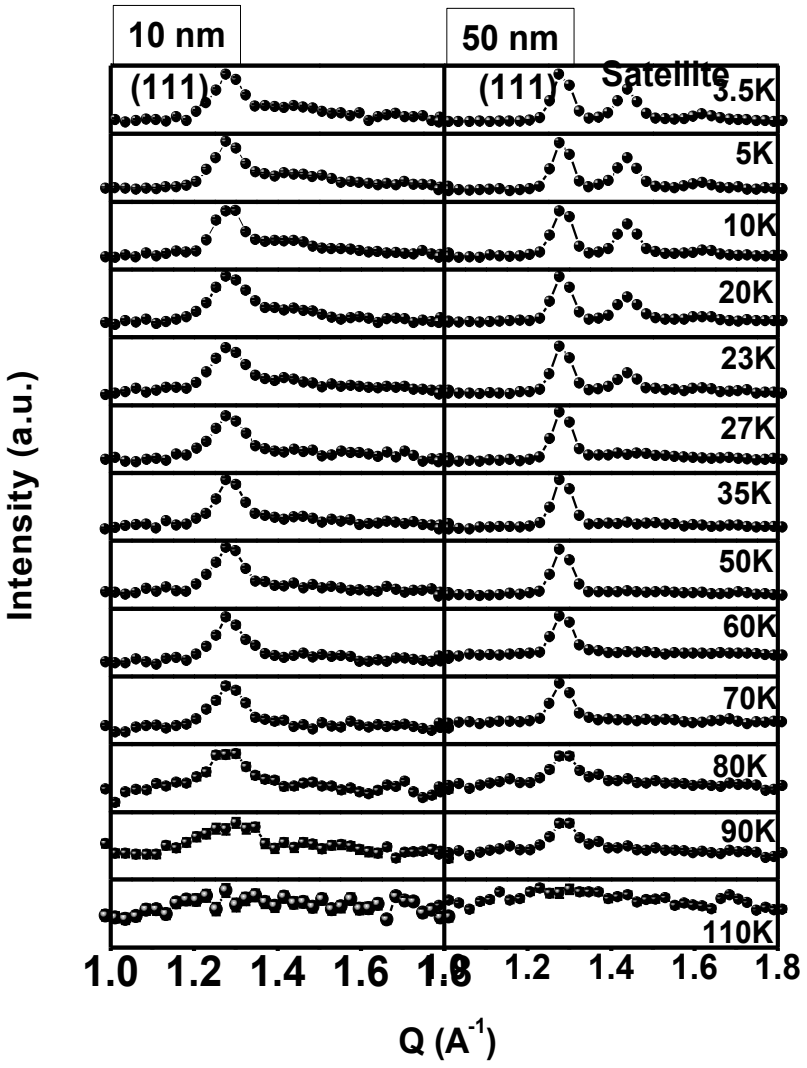

Fig.4.2.10 The temperature dependence of magnetic scattering intensities of fundamental and satellite reflections of 10 nm and 50 nm samples are shown in figure.

We have fitted asymmetric (111) by Lorentzian fitting to separate out the intensity of the satellite peak associated with the spiral order. Fig. 4.2.11 depicts the intensity of fundamental (111) peak and satellite peak with varying temperature from 100 K to 3 K.

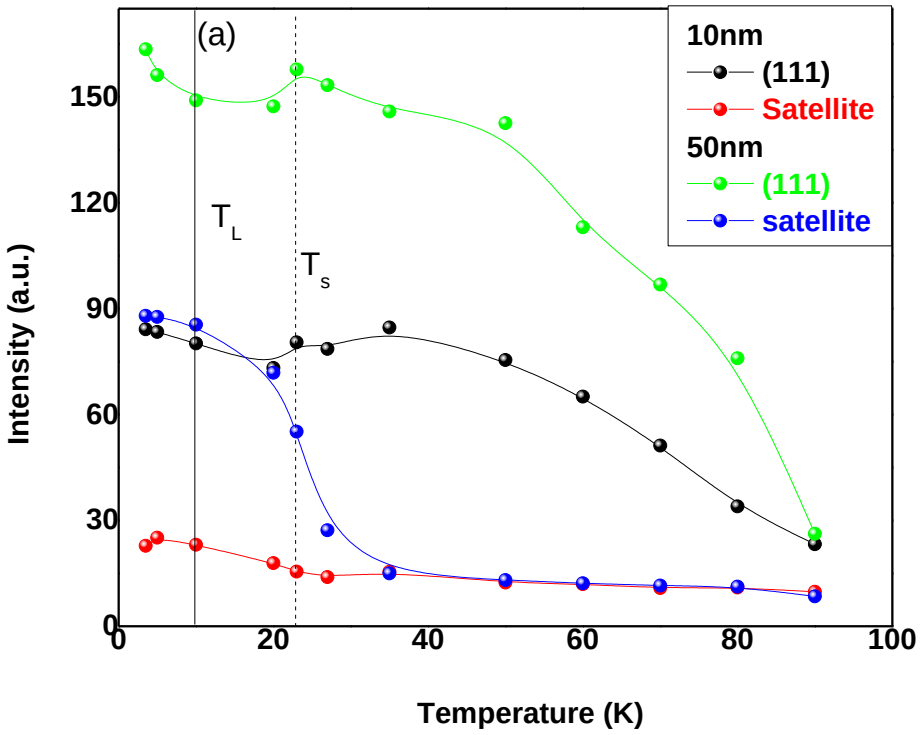

Fig. 4.2.11 Temperature dependence of integrated intensity of the fundamental magnetic (111) reflection and temperature dependence of the peak intensity of the satellite diffuse reflection of 10 nm and 50 nm samples. Solid line represents T_L and dashed line represents T_S.

Unlike bulk, intensity of the fundamental reflection in 10 nm and 50 nm samples continuously increases with decrease in temperature down to 3.5 K followed by a drop in intensity at ~23 K indicating spiral ordering temperature in both samples. The intensity of satellite peak while in 50 nm sample show a sharp transition at T_S, 10 nm sample show no significant change in intensity throughout the temperature range except at T_S and T_L. In addition to temperature dependent magnetization measurement, we show an evidence of spiral ordering in both 10 and 50 nm samples from diffused neutron scattering analysis.

We confirm that the paramagnetic to ferrimagnetic transition in both samples are continuous in contrast to bulk material. The spiral ordering is short range in 50 nm sample which is found to be diffused in 10 nm sample. Similar to our results, Tomiyasu et al., report in single crystal that below 27 K satellite peak is diffusive in nature indicating ferrimagnetic to short-range spiral ordering [Tomiyasu et al. (2004)]. No lock-in transition is reported from neutron scattering experiments done by Tomiyasu et al. We rather evidenced T_L from the change in slope in intensity of (111) at low temperature (8.5 K) in 50 nm sample and at 5 K in 10 nm sample shown as line in Fig. 4.2.11. We have calculated the correlation length of the spiral order (ξ) by taking the inverse of half width at half maxima (HWHM). The temperature dependent ξ for both samples is depicted in Fig. 4.2.12. The correlation length sharply increases as the temperature decreases and then decreases followed by a kink at T_L in 50 nm sample. Moreover, ξ is found to be 3.40 nm comparable to 3.1 nm in single crystal of $CoCr_2O_4$ [Tomiyasu et al. (2004)].

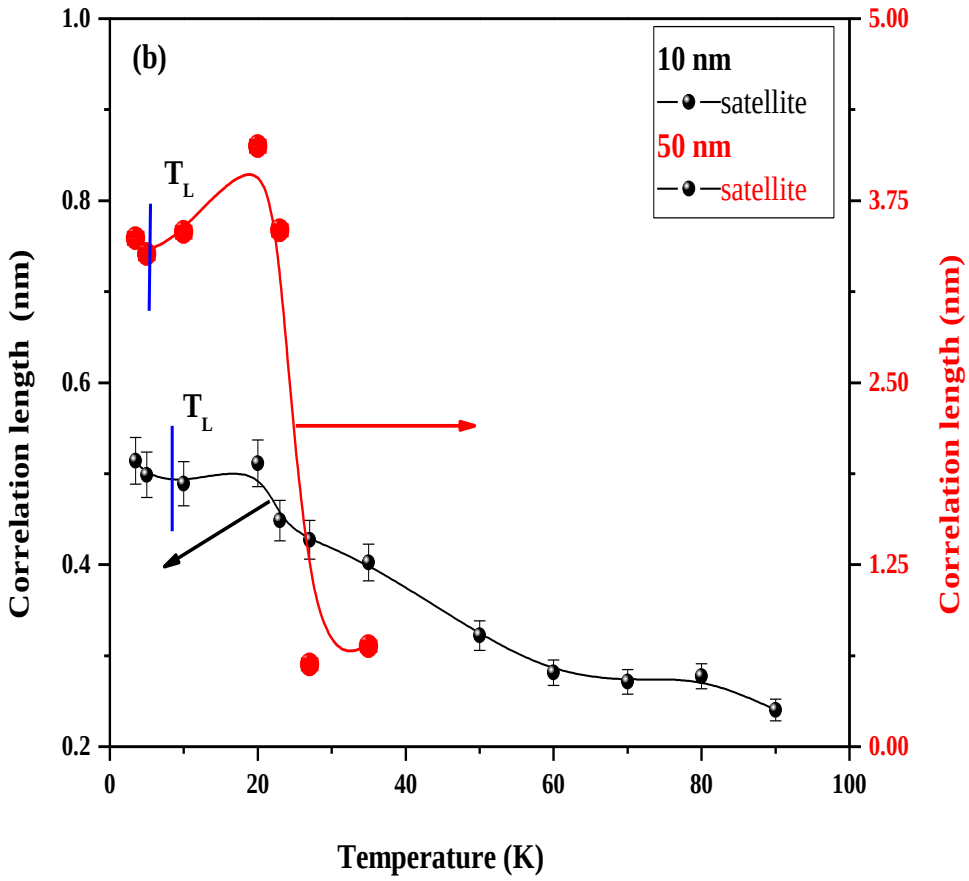

Fig. 4.2.12 Temperature dependence of the correlation length of the spiral component for 10 nm and 50 nm samples. The values are obtained by taking the inverse of the line width.

In 10 nm sample, ξ continuously increases showing a peak at T_S like in 50 nm sample and decreases further followed by a drop in ξ at around T_L. However, the correlation length does not change significantly in the 10 nm sample because of the very fine particles. We conclude that diffused neutron scattering is an effective tool to examine the magnetic transitions like T_C, T_S and T_L in nanocrystalline particles of $CoCr_2O_4$.

4.2.2.6 Conclusions

We studied the rich sequence of magnetic transitions in 10 and 50 nm samples of $CoCr_2O_4$ synthesized through conventional coprecipitation technique. Although size is reduced to nanometer range, EXAFS showed no change in cation distribution among A and B sites of $CoCr_2O_4$ unlike in spinel ferrites. For example, in bulk $CoFe_2O_4$, while Co^{2+} prefers to occupy B-sites, Fe^{3+} occupies both A- and B-sites. However, in nano size range, Co^{2+} is redistributed in both A and B-sites. Upon cooling, bulk cobalt chromite showed paramagnetic to collinear ferrimagnetic transition at Curie temperature (T_C) and to a short range non-collinear spiral ordering at T_S and finally to a lock-in transition, T_L. Though T_C and T_L varied with size of the particle, T_S remained independent confirming the persistence of strong B-B interaction even in nanoparticles. Polarized neutron scattering further showed while para to ferrimagnetic transition was continuous in both samples, spiral ordering was sharp, short range and commensurate in 50 nm sample. Splitting of ac susceptibility peak and increase in peak position with frequency, non saturation of magnetization at high field indicated the core-shell structure where core spins contributed to the ferrimagnetic phase, the disordered spins at the surface showed a spin glass behaviour. The memory experiment further confirmed the spin-glass behaviour of surface spins in 50 nm sample.